Monthly Notices of the ROYAL ASTRONOMICAL SOCIETY

MNRAS **469,** 3762–3774 (2017) doi:10.1093/mnras/stx1090
Advance Access publication 2017 May 6

The clustering of galaxies in the completed SDSS-III Baryon Oscillation Spectroscopic Survey: tomographic BAO analysis of DR12 combined sample in configuration space

Yuting Wang,[1,2★] Gong-Bo Zhao,[1,2★] Chia-Hsun Chuang,[3,4] Ashley J. Ross,[5] Will J. Percival,[2] Héctor Gil-Marín,[2] Antonio J. Cuesta,[6] Francisco-Shu Kitaura,[4] Sergio Rodriguez-Torres,[3,7,8] Joel R. Brownstein,[9] Daniel J. Eisenstein,[10] Shirley Ho,[11,12,13] Jean-Paul Kneib,[14] Matthew D. Olmstead,[15] Francisco Prada,[7] Graziano Rossi,[16] Ariel G. Sánchez,[17] Salvador Salazar-Albornoz,[17,18] Daniel Thomas,[2] Jeremy Tinker,[19] Rita Tojeiro,[20] Mariana Vargas-Magaña[21] and Fangzhou Zhu[22]

Affiliations are listed at the end of the paper

Accepted 2017 May 4. Received 2017 April 29; in original form 2016 October 17

ABSTRACT

We perform a tomographic baryon acoustic oscillations (BAOs) analysis using the two-point galaxy correlation function measured from the combined sample of Baryon Oscillation Spectroscopic Survey Data Release 12 (BOSS DR12), which covers the redshift range of $0.2 < z < 0.75$. Upon splitting the sample into multiple overlapping redshift slices to extract the redshift information of galaxy clustering, we obtain a measurement of $D_A(z)/r_d$ and $H(z)r_d$ at nine effective redshifts with the full covariance matrix calibrated using MultiDark-Patchy mock catalogues. Using the reconstructed galaxy catalogues, we obtain the precision of 1.3–2.2 per cent for $D_A(z)/r_d$ and 2.1–6.0 per cent for $H(z)r_d$. To quantify the gain from the tomographic information, we compare the constraints on the cosmological parameters using our nine-bin BAO measurements, the consensus three-bin BAO and redshift space distortion measurements at three effective redshifts in Alam et al., and the non-tomographic (one-bin) BAO measurement at a single effective redshift. Comparing the nine-bin with one-bin constraint result, it can improve the dark energy Figure of Merit by a factor of 1.24 for the Chevallier–Polarski–Linder parametrization for equation-of-state parameter $w_{\rm DE}$. The errors of w_0 and w_a from nine-bin constraints are slightly improved when compared to the three-bin constraint result.

Key words: dark energy – distance scale.

1 INTRODUCTION

The accelerating expansion of the Universe was discovered by the observation of Type Ia supernovae (Riess et al. 1998; Perlmutter et al. 1999). Understanding the physics of the cosmic acceleration is one of the major challenges in cosmology. In the framework of general relativity (GR), a new energy component with a negative pressure, dubbed dark energy (DE), can be the source driving the cosmic acceleration. Observations reveal that the DE component dominates the current Universe (Weinberg et al. 2013). However, the nature of DE remains unknown. Large cosmological surveys, especially for galaxy redshift surveys, can provide key observational support for the study of DE.

Galaxy redshift surveys are used to map the large-scale structure of the Universe, and extract the signal of baryon acoustic oscillation (BAO). The BAO, produced by the competition between gravity and radiation due to the couplings between baryons and photons before the cosmic recombination, leave an imprint on the distribution of galaxies at late times. After the photons decouple, the acoustic oscillations are frozen and correspond to a characteristic scale, determined by the comoving sound horizon at the drag epoch, $r_d \sim 150$ Mpc. This feature corresponds to an excess in the two-point correlation function, or a series of wiggles in

★ E-mail: ytwang@nao.cas.cn (YW); gbzhao@nao.cas.cn (G-BZ)

the power spectrum. The acoustic scale is regarded as a standard ruler to measure the cosmic expansion history, and to constrain cosmological parameters (Eisenstein et al. 2005). If assuming an isotropic galaxy clustering, the combined volume distance, $D_V(z) \equiv [cz(1+z)^2 D_A(z)^2 H^{-1}(z)]^{1/3}$, where $H(z)$ is the Hubble parameter and $D_A(z)$ is the angular diameter distance, can be measured using the angle-averaged two-point correlation function, $\xi_0(s)$ (Eisenstein et al. 2005; Kazin et al. 2010; Beutler et al. 2011; Blake et al. 2011) or power spectrum $P_0(k)$ (Tegmark et al. 2006; Percival et al. 2007; Reid et al. 2010). However, in principle the clustering of galaxies is anisotropic, the BAO scale can be measured in the radial and transverse directions to provide the Hubble parameter, $H(z)$, and angular diameter distance, $D_A(z)$, respectively. As proposed by Padmanabhan & White 2008, the 'multipole' projection of the full 2D measurement of power spectrum, $P_\ell(k)$, were used to break the degeneracy of $H(z)$ and $D_A(z)$. This multipole method was applied into the correlation function (Chuang & Wang 2012, 2013; Xu et al. 2013). Alternative 'wedge' projection of correlation function, $\xi_{\Delta\mu}(s)$, was used to constrain parameters, $H(z)$ and $D_A(z)$ (Kazin, Sánchez & Blanton 2012; Kazin et al. 2013). In Anderson et al. (2014), the anisotropic BAO analysis was performed using these two projections of correlation function from SDSS-III Baryon Oscillation Spectroscopic Survey (BOSS) DR10 and DR11 samples.

The BOSS (Dawson et al. 2013), which is part of SDSS-III (Eisenstein et al. 2011), has provided the Data Release 12 (Alam et al. 2015). With a redshift cut, the whole samples are split into the 'low-redshift' samples (LOWZ) in the redshift range $0.15 < z < 0.43$ and 'constant stellar mass' samples (CMASS) in the redshift range $0.43 < z < 0.7$. Using these catalogues, the BAO peak position was measured at two effective redshifts, $z_{\rm eff} = 0.32$ and $z_{\rm eff} = 0.57$, in the multipoles of correlation function (Cuesta et al. 2016) or power spectrum (Gil-Marín et al. 2016). Chuang et al. (2016) proposed to divide each sample of LOWZ and CMASS into two independent redshift bins, thus to test the extraction of redshift information from galaxy clustering. They performed the measurements on BAO and growth rate at four effective redshifts, $z_{\rm eff} = 0.24, 0.37, 0.49$ and 0.64 (Chuang et al. 2016).

The completed data release of BOSS will provide a combined sample, covering the redshift range from 0.2 to 0.75. The sample is divided into three redshift bins, i.e., two independent redshift bins, $0.2 < z < 0.5$ and $0.5 < z < 0.75$, and an overlapping redshift bin, $0.4 < z < 0.6$. The BAO signal is measured at the three effective redshifts, $z_{\rm eff} = 0.38, 0.51$ and 0.61 using the configuration-space correlation function (Vargas-Magaña et al. 2016; Ross et al. 2017) or Fourier-space power spectrum (Beutler et al. 2017a).

As the tomographic information of galaxy clustering is important to constrain the property of DE (Salazar-Albornoz et al. 2014; Zhao et al. 2017a), we will extract the information of redshift evolution from the combined catalogue as much as possible. To achieve this, we adopt the binning method. The binning scheme is determined through the forecasting result using Fisher matrix method. We split the whole sample into *nine overlapping* redshift bins to make sure that the measurement precision of the isotropic BAO signal is better than 3 per cent in each bin. We perform the measurements on the an/isotropic BAO positions in the *nine overlapping* bins using the correlation functions of the pre- and post-reconstruction catalogues. To test the constraining power of our tomographic BAO measurements, we perform the fitting of cosmological parameters.

The analysis is part of a series of papers analysing the clustering of the completed BOSS DR12 (Alam et al. 2016; Chuang et al. 2016; Salazar-Albornoz et al. 2017; Vargas-Magaña et al. 2016; Beutler et al. 2017a,b; Grieb et al. 2017; Ross et al. 2017; Sánchez et al. 2017a,b; Zhao et al. 2017b). The same tomographic BAO analysis is performed using galaxy power spectrum in Fourier space (Zhao et al. 2017b). Another tomographic analysis is performed using the angular correlation function in many thin redshift shells and their angular cross-correlations in the companion paper, Salazar-Albornoz et al. (2017), to extract the time evolution of the clustering signal.

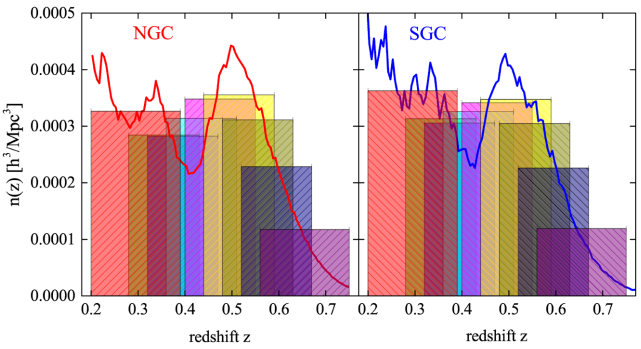

Figure 1. The overlapping histograms in different colours are the average number densities in nine redshift bins, which is used to do the forecasts. The solid lines are the number densities for the NGC/SGC samples.

In Section 2, we introduce the data and mocks used in this paper. We present the forecast result in Section 3. In Section 4, we describe the methodology to measure the BAO signal using multipoles of correlation function. In Section 5, we constrain cosmological models using the BAO measurement from the post-reconstructed catalogues. Section 6 is devoted to the conclusion. In this paper, we use a fiducial ΛCDM cosmology with the parameters: $\Omega_m = 0.307$, $\Omega_b h^2 = 0.022$, $h = 0.6777$, $n_s = 0.96$, $\sigma_8 = 0.8288$. The comoving sound horizon in this cosmology is $r_d^{\rm fid} = 147.74$ Mpc.

2 DATA AND MOCKS

We use the completed catalogue of BOSS DR12, which covers the redshift range from 0.2 to 0.75. In the North Galactic Cap (NGC), 864 923 galaxies over the effective coverage area of 5923.90 deg^2 are observed and the South Galactic Cap (SGC) contains 333 081 with the effective coverage area of 2517.65 deg^2. The volume density distribution from observation is shown in solid curves of Fig. 1.

In order to correct for observational effects, the catalogue is given a set of weights, including weights for the redshift failure, $w_{\rm zf}$, close pair due to fibre collisions, $w_{\rm cp}$ and for systematics, $w_{\rm sys}$. In addition, the FKP weight to minimize the variance in the clustering measurement combining regions (Feldman, Kaiser & Peacock 1994) is added

$$w_{\rm FKP} = \frac{1}{1 + n(z)P_0}, \tag{1}$$

where $n(z)$ is the number density of galaxies, and P_0 is set to $10\,000\,h^{-3}$ Mpc^3. Thus each galaxy is counted by adding a total weight as below

$$w_{\rm tot} = w_{\rm FKP} w_{\rm sys}(w_{\rm cp} + w_{\rm zf} - 1). \tag{2}$$

The details about the observational systematic weights are described in Ross et al. (2017).

The correlation function is measured by comparing the galaxy distribution to a randomly distributed catalogue, which is reconstructed with the same radial selection function as the real catalogue,

but without clustering structure. We use a random catalogue consisting of 50 times random galaxies of the observed sample.

During the cosmic evolution, nonlinear structure formation and redshift space distortions (RSD) can weaken the significance of the BAO peak thus degrade the precision of BAO measurements. The BAO signal can be boosted to some extent by the reconstruction procedure, which effectively moves the galaxies to the positions as if there was no RSD and nonlinear effects (Eisenstein et al. 2007b). We will also present BAO measurements using the catalogue, which is reconstructed through the reconstruction algorithm as described in Padmanabhan et al. (2012).

Mock galaxy catalogues are required to determine the data covariance matrix, and to test the methodology. We use the MultiDark-Patchy mock catalogues (Kitaura et al. 2016). The mock catalogues are constructed to match the observed data on the angular selection function, redshift distribution and clustering statistics (*e.g.* two-point and three-point correlation functions). We utilize 2045 mock catalogues for the pre-reconstruction, and 1000 mocks for the post-reconstruction. We perform the measurement for each mock catalogue, then estimate the covariance matrix of data correlation function using the method proposed in Percival et al. (2014).

3 BAO FORECASTS

We first determine the binning scheme through the Fisher matrix method. We use the Fisher matrix formulae for predicting the BAO distance parameters in (Tegmark 1997; Seo & Eisenstein 2007). Starting with the galaxy power spectrum, $P(k, \mu)$, the Fisher matrix is

$$F_{ij} = \int_{-1}^{1}\int_{k_{\rm min}}^{k_{\rm max}} \frac{\partial \ln P(k,\mu)}{\partial p_i}\frac{\partial \ln P(k,\mu)}{\partial p_j} V_{\rm eff}(k,\mu)\frac{k^2\,{\rm d}k{\rm d}\mu}{8\pi^2},$$
$$\simeq V_{\rm sur}\int_{-1}^{1}{\rm d}\mu\int_{k_{\rm min}}^{k_{\rm max}} \frac{\partial \ln P_b(k,\mu)}{\partial p_i}\frac{\partial \ln P_b(k,\mu)}{\partial p_j}$$
$$\cdot\left[\frac{nb(z)^2(1+\beta\mu^2)^2P_{\rm m}^{\rm lin}(k,z)}{nb(z)^2(1+\beta\mu^2)^2P_{\rm m}^{\rm lin}(k,z)+1}\right]^2\frac{k^2{\rm d}k}{8\pi^2} \quad (3)$$

where $P_b(k, \mu)$ denotes the power spectrum containing the BAO feature (Seo & Eisenstein 2007), $b(z)$ is the bias factor, β is the linear redshift distortion parameter, $P_{\rm m}^{\rm lin}(k, z)$ is the linear matter power spectrum at redshift z and p_i are the parameters to be estimated. Here, we set $k_{\rm min} = 2\pi/V_{\rm sur}^{1/3}\,h\,{\rm Mpc}^{-1}$ and $k_{\rm max} = 0.3\,h\,{\rm Mpc}^{-1}$.

In order to ensure that the isotropic BAO measurement precision in each bin is better than 3 per cent, we split the whole redshift range, i.e. [0.2, 0.75] into nine overlapping bins. The width of the first and last bins is 0.19, and other bins have the same bin width, i.e. $\Delta z = 0.15$.

In Table 1, we present the nine overlapping redshift ranges, the effective redshifts and numbers of the samples in the NGC and SGC. In Fig. 1, the overlapping histograms denote the average number density in each bin.

Combining the results of NGC and SGC samples as

$$F_{ij}^{\rm NGC+SGC} = F_{ij}^{\rm NGC} + F_{ij}^{\rm SGC}, \quad (4)$$

we present the forecast result on the precision of the BAO distance parameters, including the angular diameter distance $D_A(z)$, Hubble parameter $H(z)$ and volume distance $D_V(z)$ in Table 2. It is seen that the isotropic BAO prediction in each bin can reach, $\sigma_{D_V}/D_V <$ 3 per cent. With the '50 per cent' reconstructed efficiency, which means that the nonlinear damping scales, $\Sigma_\perp$ and $\Sigma_\parallel$, are reduced by a factor 0.5 and there is the remaining 50 per cent nonlinearity, the isotropic BAO precision is within 0.8–1.2 per cent.

The predictions on the precision of anisotropic BAO parameters are within 1.8–2.9 per cent for the angular diameter distance and 4.2–7.1 per cent for the Hubble parameter without the reconstruction. Considering the '50 per cent' reconstruction, the best prediction can reach 1.1 per cent for $D_A(z)$ and 2.1 per cent for $H(z)$. The contour plot of $D_A(z)$ and $H(z)$ within 2σ error is displayed in Fig. 2, where the black points are the fiducial values. The upper panel in Fig. 2 shows the forecast result without reconstruction, and the lower panel presents the '50 per cent' reconstructed result.

Table 1. The nine overlapping redshift bins, the effective redshift and the number of samples in each bin.

z bins	$z_{\rm eff}$	NGC	SGC
$0.20 < z < 0.39$	0.31	208 517	89 242
$0.28 < z < 0.43$	0.36	194 754	81 539
$0.32 < z < 0.47$	0.40	230 388	93 825
$0.36 < z < 0.51$	0.44	294 749	115 029
$0.40 < z < 0.55$	0.48	370 429	136 117
$0.44 < z < 0.59$	0.52	423 716	154 486
$0.48 < z < 0.63$	0.56	410 324	149 364
$0.52 < z < 0.67$	0.59	331 067	121 145
$0.56 < z < 0.75$	0.64	243 763	91 170

Table 2. The forecast results on the BAO distance parameters without reconstruction (and '50 per cent' reconstruction) using the combination of NGC and SGC samples.

$z_{\rm eff}$	σ_{D_A}/D_A	σ_H/H	σ_{D_V}/D_V
0.31	0.0289 (159)	0.0705 (309)	0.0236 (114)
0.36	0.0281 (159)	0.0681 (307)	0.0229 (113)
0.40	0.0254 (145)	0.0616 (281)	0.0207 (104)
0.44	0.0226 (130)	0.0553 (253)	0.0185 (093)
0.48	0.0203 (118)	0.0502 (230)	0.0167 (085)
0.52	0.0188 (110)	0.0464 (214)	0.0155 (079)
0.56	0.0180 (108)	0.0441 (208)	0.0147 (077)
0.59	0.0183 (113)	0.0436 (214)	0.0147 (080)
0.64	0.0187 (122)	0.0418 (222)	0.0144 (085)

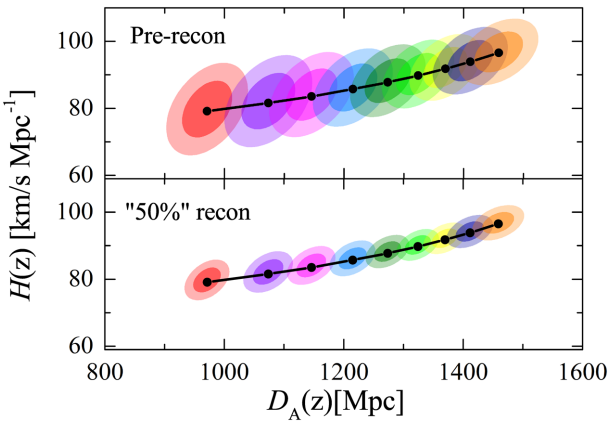

Figure 2. The 68 and 95 per cent CL contour plots of the transverse and radial distance parameters, $D_A(z)$ and $H(z)$, in nine redshift bins are shown one by one from left to right. The upper panel shows the result without the reconstruction, and the lower panel is the result with '50 per cent' reconstructed efficiency.

4 BAO MEASUREMENTS

4.1 The estimator for the two-pt correlation function

We measure the correlation function of the combined sample using the Landy & Szalay (1993) estimator:

$$\xi(s,\mu) = \frac{\mathrm{DD}(s,\mu) - 2\mathrm{DR}(s,\mu) + \mathrm{RR}(s,\mu)}{\mathrm{RR}(s,\mu)}, \quad (5)$$

where DD, DR and RR are the weighted data–data pair counts, data–random pair counts and random–random pair counts with the separation, s, and the cosine of the angle of the pair to the line of sight, μ.

The multipole projections of the correlation function can be calculated through

$$\xi_l(s) = \frac{2l+1}{2}\int_{-1}^{1} \mathrm{d}\mu\, \xi(s,\mu)\mathcal{L}_\ell(\mu), \quad (6)$$

where $\mathcal{L}_\ell(\mu)$ is the Legendre polynomial.

We also measure the correlation function of the reconstructed catalogue using the Landy & Szalay (1993) estimator:

$$\xi(s,\mu) = \frac{\mathrm{DD}(s,\mu) - 2\mathrm{DS}(s,\mu) + \mathrm{SS}(s,\mu)}{\mathrm{RR}(s,\mu)}, \quad (7)$$

here we used the shifted data and randoms for DD, DS and SS.

The measured monopole and quadrupole of correlation function from the pre-reconstruction data and mocks in each redshift bin are shown in the left-hand panel of Fig. 3 and the post-reconstruction measurement results are shown in the right-hand panel of Fig. 3, where the red squares with 1σ error bar are the measurements of monopole from data. The red shaded regions correspond to the standard deviation from the mocks around the average. The blue points with 1σ error bar are the data measurements of quadrupole, and the blue shaded regions denote the average with a standard deviation from the mocks.

The 2D correlation functions measured in nine redshift bins using the pre-reconstructed and post-reconstructed catalogues are plotted in Fig. 4, where the BAO ring in each redshift slice is visualized. As expected, the BAO ring becomes clear after reconstruction.

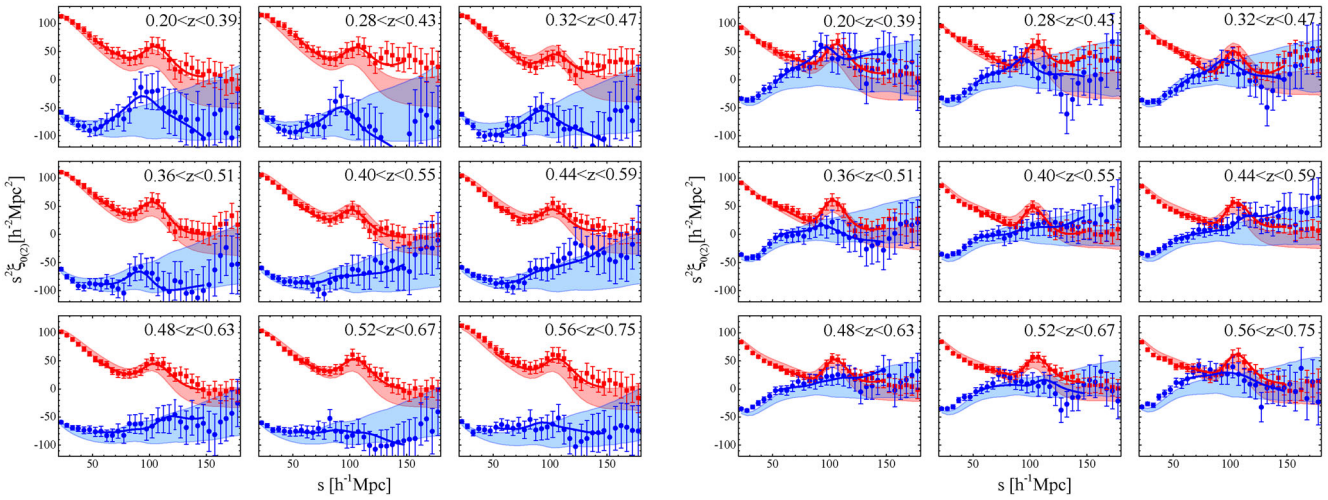

Figure 3. The measured monopole and quadrupole of correlation function using the pre-reconstructed catalogue (left-hand panel) and post-reconstructed catalogue (right-hand panel) in each redshift bin: in each panel, the red square with 1σ error bar is the measured monopole and the red shaded band is the average of monopoles from mocks with a standard deviation. The blue point with 1σ error bar is the measured quadrupole and the blue shaded band is the average of quadrupoles from mocks with a standard deviation. The solid lines show the fitting results.

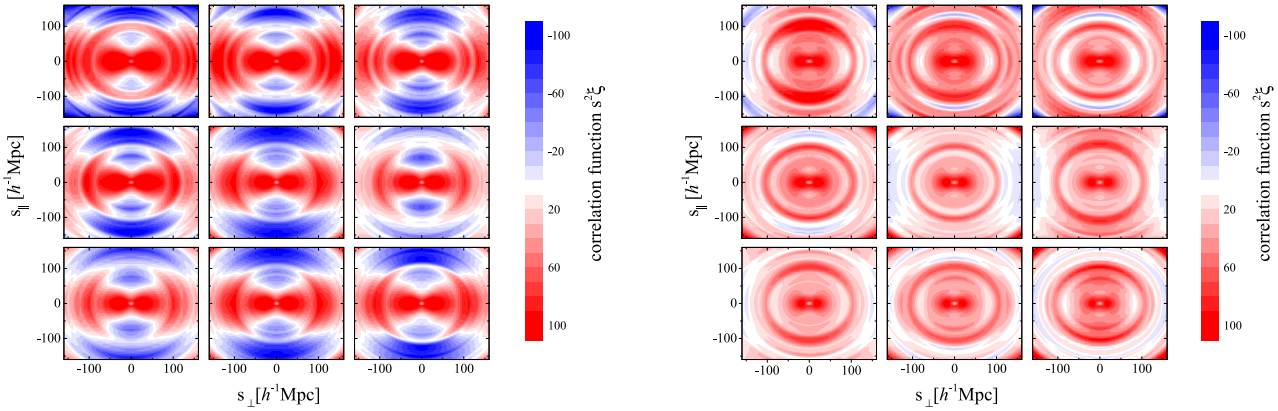

Figure 4. The 2D pre-reconstruction correlation functions (left-hand panel) and post-reconstruction correlation functions (right-hand panel) in nine redshift bins, which is assembled using the measured monopole and quadrupole from the NGC and SGC samples, i.e. $\xi(s,\mu) = \xi_0(s)\mathcal{L}_0(\mu) + \xi_2(s)\mathcal{L}_2(\mu)$, here $s_\parallel = s\mu$ and $s_\perp = s\sqrt{1-\mu^2}$.

4.2 The template

The isotropic BAO position is parametrized by the scale dilation parameter,

$$\alpha \equiv \frac{D_V(z) r_{d,\rm fid}}{D_V^{\rm fid}(z) r_d}. \tag{8}$$

We adopt the template for the correlation function in the isotropic case (Eisenstein, Seo & White 2007a)

$$\xi^{\rm mod}(s) = \int \frac{k^2 {\rm d}k}{2\pi^2} P_{\rm dw}^{\rm mod}(k) F(k, \Sigma_s) j_0(ks), \tag{9}$$

where the damping term is given by

$$F(k, \Sigma_s) = \frac{1}{(1 + k^2\Sigma_s^2/2)^2}. \tag{10}$$

Here, we set the parameter $\Sigma_s = 4\,h^{-1}$ Mpc, which is the same as used in Ross et al. (2017). The de-wiggled power spectrum, $P_{\rm dw}^{\rm mod}(k)$, is given by

$$P_{\rm dw}^{\rm mod}(k) = P^{\rm nw}(k) + \left[P^{\rm lin}(k) - P^{\rm nw}(k)\right] {\rm e}^{-\frac{1}{2}k^2\Sigma_{\rm nl}^2}, \tag{11}$$

where $P^{\rm nw}(k)$ is the 'no-wiggle' power spectrum, where the BAO feature is erased, which is obtained using the fitting formulae in Eisenstein & Hu (1998). The linear power spectrum $P^{\rm lin}(k)$ is calculated by CAMB[1] (Lewis, Challinor & Lasenby 2000). $\Sigma_{\rm nl}$ in the Gaussian term is a damping parameter.

Then, allowing an unknown bias factor B_ξ, which rescales the amplitude of the input template, the correlation function is given by

$$\xi^{\rm fit}(s) = B_\xi^2 \xi^{\rm mod}(\alpha s) + A^\xi(s), \tag{12}$$

which includes the polynomial terms for systematics

$$A^\xi(s) = \frac{a_1}{s^2} + \frac{a_2}{s} + a_3. \tag{13}$$

Before doing the fitting, we normalize the model to the data at the scale $s = 50\,h^{-1}$ Mpc, as done in Xu et al. (2013) and Anderson et al. (2014). While performing the fitting, we add a Gaussian prior on $\log(B_\xi^2) = 0 \pm 0.4$ (Xu et al. 2013; Anderson et al. 2014). So in the isotropic case, we have five free parameters, i.e. $[\log(B_\xi^2), \alpha, a_1, a_2, a_3]$.

The BAO feature can be measured in both the transverse and line-of-sight directions. This can be parametrized by $\alpha_\perp$ and $\alpha_{||}$, respectively

$$\alpha_\perp = \frac{D_A(z) r_d^{\rm fid}}{D_A^{\rm fid}(z) r_d}, \quad \alpha_\parallel = \frac{H^{\rm fid}(z) r_d^{\rm fid}}{H(z) r_d}. \tag{14}$$

The anisotropic correlation function is modelled as a transform of the 2D power spectrum,

$$P(k, \mu) = (1 + \beta\mu^2)^2 F(k, \mu, \Sigma_s) P_{\rm dw}(k, \mu), \tag{15}$$

where the $(1 + \beta\mu^2)^2$ term corresponds to the Kaiser model for large-scale RSD (Kaiser 1987). For the reconstruction, this term is replaced by $[1 + \beta\mu^2(1 - S(k))]^2$ with the smoothing, $S(k) = e^{-k^2\Sigma_r^2/2}$ and $\Sigma_r = 15\,h^{-1}$ Mpc (Seo et al. 2016). The term

$$F(k, \mu, \Sigma_s) = \frac{1}{(1 + k^2\mu^2\Sigma_s^2/2)^2} \tag{16}$$

is introduced to model the small-scale FoG effect. The 2D de-wiggled power spectrum, compared to equation (11), becomes

$$P_{\rm dw}(k, \mu) = [P_{\rm lin}(k) - P_{\rm nw}(k)] \times \exp\left[-\frac{k^2\mu^2\Sigma_\parallel^2 + k^2(1-\mu^2)\Sigma_\perp^2}{2}\right] + P_{\rm nw}(k), \tag{17}$$

here the Gaussian damping term is also anisotropic. $\Sigma_\parallel$ and $\Sigma_\perp$ are the line-of-sight and transverse components of $\Sigma_{\rm nl}$, i.e. $\Sigma_{\rm nl}^2 = (\Sigma_\parallel^2 + 2\Sigma_\perp^2)/3$. Here, we set $\Sigma_\parallel = 4\,h^{-1}$ Mpc and $\Sigma_\perp = 2.5\,h^{-1}$ Mpc for the post-reconstruction and $\Sigma_\parallel = 10\,h^{-1}$ Mpc and $\Sigma_\perp = 6\,h^{-1}$ Mpc for the pre-reconstruction (Ross et al. 2017).

Given the 2D power spectrum $P(k, \mu)$, which can be decomposed into Legendre moments, then the multipoles of power spectrum are

$$P_\ell(k) = \frac{2\ell + 1}{2} \int_{-1}^{1} P(k, \mu) \mathcal{L}_\ell(\mu)\, {\rm d}\mu, \tag{18}$$

which can be transformed to the multipoles of correlation function by

$$\xi_\ell(s) = \frac{i^\ell}{2\pi^2} \int k^2 P_\ell(k) j_\ell(ks)\, {\rm d}k. \tag{19}$$

Using the Legendre polynomials, we have

$$\xi(s, \mu) = \sum_\ell \xi_\ell(s) \mathcal{L}_\ell(\mu). \tag{20}$$

Then the model multipoles of correlation function are

$$\xi_\ell(s, \alpha_\perp, \alpha_\parallel) = \frac{2\ell + 1}{2} \int_{-1}^{1} \xi(s', \mu') \mathcal{L}_\ell(\mu)\, {\rm d}\mu, \tag{21}$$

where $s' = s\sqrt{\mu^2\alpha_\parallel^2 + (1-\mu^2)\alpha_\perp^2}$ and $\mu' = \mu\alpha_\parallel \Big/ \sqrt{\mu^2\alpha_\parallel^2 + (1-\mu^2)\alpha_\perp^2}$ are the separation between two galaxies and the cosine of the angle of the pair to the line of sight in the true cosmology, respectively.

In addition, we use a bias parameter B_0 to adjust the amplitude of the input template and include the model for systematics using the polynomial terms

$$A_\ell(s) = \frac{a_{\ell,1}}{s^2} + \frac{a_{\ell,2}}{s} + a_{\ell,3}. \tag{22}$$

So we fit the data using the model multipoles

$$\xi_0^{\rm mod}(s) = B_0 \xi_0(s, \alpha_\perp, \alpha_\parallel) + A_0(s), \tag{23}$$

$$\xi_2^{\rm mod}(s) = \xi_2(s, \alpha_\perp, \alpha_\parallel) + A_2(s). \tag{24}$$

As in the isotropic case, the monopole template is normalized to the measurement at $s = 50\,h^{-1}$ Mpc. So in the anisotropic case, we have 10 free parameters, i.e. $[\alpha_\perp, \alpha_{||}, \log(B_0^2), \beta, a_{\ell,1-3}]$. While performing the fitting, a Gaussian prior on $\log(B_0^2) = 0 \pm 0.4$ is applied. We also add a Gaussian prior for the RSD parameter, i.e. $\beta = 0.4 \pm 0.2$ (Anderson et al. 2014).

4.3 Covariance matrix

When fitting the BAO parameters, $\boldsymbol{p}$, we use the MCMC to search for the minimum χ^2,

$$\chi^2(\mathbf{p}) \equiv \sum_{i,j}^{\ell,\ell'} \left[\xi_\ell^{\rm th}(s_i, \mathbf{p}) - \xi_\ell(s_i)\right] F_{ij}^{\ell,\ell'} \left[\xi_{\ell'}^{\rm th}(s_j, \mathbf{p}) - \xi_{\ell'}(s_j)\right].$$

[1] http://camb.info

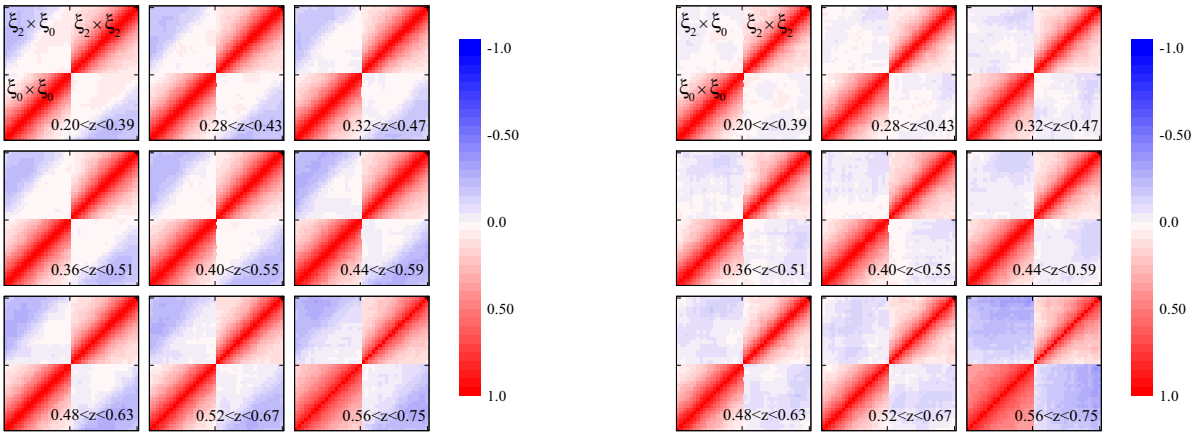

Figure 5. The correlation matrix for cases of pre-reconstruction (left-hand panel) and post-reconstruction (right-hand panel). For each block in each panel, we show correlation for 20 bins linearly even spaced in separation s between 50 and 150 Mpc h^{-1}.

where $F_{ij}^{\ell,\ell'}$ is the inverse of the covariance matrix, $C_{ij}^{\ell,\ell'}$, which is estimated using mock catalogues,

$$C_{ij}^{\ell,\ell'} = \frac{1}{N-1}\sum_k \left[\xi_\ell^k(s_i) - \bar{\xi}_\ell(s_i)\right]\left[\xi_{\ell'}^k(s_j) - \bar{\xi}_{\ell'}(s_j)\right], \quad (25)$$

where the average multipoles is given by

$$\bar{\xi}_\ell(s_i) = \frac{1}{N}\sum_k \xi_\ell^k(s_i), \quad (26)$$

here N is the number of mocks: $N = 2045$ in the pre-reconstruction case and $N = 1000$ in the post-reconstruction case. The unbiased estimation for the inverse covariance matrix is given by

$$\widetilde{C}_{ij}^{-1} = \frac{N - N_b - 2}{N-1} C_{ij}^{-1}. \quad (27)$$

where N_b is the number of the scale bins. In order to include the error propagation from the error in the covariance matrix into the fitting parameters (Percival et al. 2014), we rescale the covariance matrix, $\widetilde{C}_{ij}$, by

$$M = \sqrt{\frac{1 + B(N_b - N_p)}{1 + A + B(N_p + 1)}} \quad (28)$$

here N_p is the number of the fitting parameters, and

$$A = \frac{2}{(N - N_b - 1)(N - N_b - 4)}, \quad (29)$$

$$B = \frac{N - N_b - 2}{(N - N_b - 1)(N - N_b - 4)}. \quad (30)$$

The correlation matrices, which are the normalized covariance matrices so that all the diagonal elements are unity, for the pre-reconstruction and post-reconstruction in each redshift bin are plotted in the left- and right-hand panel of Fig. 5, respectively. As shown, there is less auto-correlation of multipoles and cross-correlation between multipoles for the post-reconstruction case.

5 TESTS ON MOCK CATALOGUES

We present the mock tests for the BAO analysis using 1000 pre-reconstructed and post-reconstructed mocks. We perform the isotropic and anisotropic BAO measurements using each individual mock catalogue in both cases. The results are shown in Table 3, where we list the average of fitting value from each mock, standard derivations and the average of 1σ error for the parameters, α, $\alpha_\perp$ and $\alpha_\parallel$. The fiducial cosmology we use here corresponds to the input cosmology of the mocks, therefore we expect that the average values of parameters α, $\alpha_\perp$ and $\alpha_\parallel$ are equal to 1.

Our recovered parameter values in nine redshift bins are well consistent with the input cosmology. For the isotropic results, we find that the greatest bias in α for the pre-reconstruction result is less than 0.4 per cent, and is less than 0.2 per cent in the post-reconstruction case. The 1D distribution of the parameter α from mocks is shown in the histograms of Fig. 6, where the blue histograms are the pre-reconstruction results, and the red histograms are the post-reconstruction results. As expected, the BAO signals measured from the post-reconstructed mocks are more significant, as shown in the scatter plots of Fig. 7, where each point in the plot corresponds to the 1σ error value from each pre- and post-reconstructed mock. For the anisotropic results, on average the biases in the anisotropic parameters are less than 0.5 per cent. We display the 1D distributions of the parameters, $\alpha_\perp$ and $\alpha_\parallel$ from mocks in the histograms of Fig. 8. The scatter plots for the parameters, $\alpha_\perp$ and $\alpha_\parallel$ are shown in Fig. 9.

6 RESULTS

6.1 Isotropic BAO measurements

The correlation functions are measured with the bin width of 5 h^{-1} Mpc, as shown in Fig. 3. We perform the fitting in the range 50–150 h^{-1} Mpc.

We present the constraints on the isotropic BAO scale in all redshift bins in Table 4. Using the values of $D_V^{\rm fid}(z)/r_d^{\rm fid}$ for the fiducial cosmology, we derive the constraint on $D_V(z)/r_d$, as listed in the last two columns of Table 4. The measurement precision on $D_V(z)/r_d$ from the pre-reconstruction catalogue can reach 1.8–3.3 per cent. For the post-reconstruction, the precision is improved to be 1.1–1.8 per cent.

The improvement on the measurement precision of α after reconstruction can be seen in Fig. 10, where we show our tomographic measurements in terms of the redshift in blue squares. The pre-reconstruction constraints are plotted in upper panel, and the lower panel shows the result after reconstruction.

Table 3. The statistics of the isotropic and anisotropic BAO fittings using the pre-reconstructed and post-reconstructed mocks. $\langle\alpha\rangle$, $\langle\alpha_\perp\rangle$ and $\langle\alpha_\parallel\rangle$ are the average of the fitting mean value from each mock. S_α, $S_{\alpha_\perp}$ and $S_{\alpha_\parallel}$ are the standard derivation of the parameters α, $\alpha_\perp$ and $\alpha_\parallel$, respectively. $\langle\sigma_\alpha\rangle$, $\langle\sigma_{\alpha_\perp}\rangle$ and $\langle\sigma_{\alpha_\parallel}\rangle$ correspond to the average of 1σ error of these three parameters from each mock.

$z_{\rm eff}$	$\langle\alpha\rangle$	S_α	$\langle\sigma_\alpha\rangle$	$\langle\chi^2\rangle$/dof	$\langle\alpha_\perp\rangle$	$S_{\alpha_\perp}$	$\langle\sigma_{\alpha_\perp}\rangle$	$\langle\alpha_\parallel\rangle$	$S_{\alpha_\parallel}$	$\langle\sigma_{\alpha_\parallel}\rangle$	$\langle\chi^2\rangle$/dof
Pre-reconstruction											
0.31	0.996	0.033	0.036	15.1/15	0.997	0.042	0.044	0.992	0.064	0.078	30.3/30
0.36	0.997	0.031	0.034	15.1/15	0.995	0.040	0.043	0.995	0.064	0.077	30.3/30
0.40	1.000	0.029	0.031	15.0/15	0.998	0.038	0.039	0.996	0.064	0.073	30.2/30
0.44	1.001	0.024	0.027	15.2/15	0.999	0.033	0.034	0.998	0.061	0.068	30.3/30
0.48	1.003	0.022	0.024	15.2/15	0.999	0.030	0.030	1.003	0.061	0.062	30.2/30
0.52	1.002	0.021	0.022	15.2/15	0.999	0.028	0.029	1.001	0.059	0.060	30.1/30
0.56	1.002	0.020	0.022	15.1/15	0.998	0.029	0.029	1.003	0.058	0.059	29.9/30
0.59	1.001	0.021	0.023	15.4/15	0.998	0.031	0.031	1.001	0.059	0.061	30.3/30
0.64	1.002	0.022	0.025	15.4/15	0.999	0.033	0.034	1.000	0.059	0.062	30.5/30
Post-reconstruction											
0.31	0.999	0.019	0.021	15.2/15	0.993	0.028	0.027	0.998	0.049	0.050	29.7/30
0.36	0.999	0.018	0.021	15.2/15	0.992	0.028	0.026	0.998	0.050	0.049	29.7/30
0.40	0.999	0.017	0.019	15.2/15	0.994	0.026	0.025	0.999	0.048	0.045	29.8/30
0.44	0.999	0.015	0.016	15.2/15	0.994	0.022	0.021	1.001	0.040	0.038	30.0/30
0.48	1.001	0.013	0.015	15.2/15	0.995	0.019	0.018	1.003	0.036	0.035	30.1/30
0.52	1.001	0.013	0.014	15.3/15	0.996	0.017	0.017	1.005	0.034	0.032	30.1/30
0.56	1.002	0.012	0.013	15.3/15	0.995	0.018	0.017	1.006	0.034	0.032	30.1/30
0.59	1.001	0.013	0.014	15.3/15	0.996	0.019	0.019	1.003	0.037	0.035	29.9/30
0.64	1.001	0.015	0.017	15.2/15	0.995	0.022	0.022	1.004	0.040	0.040	29.9/30

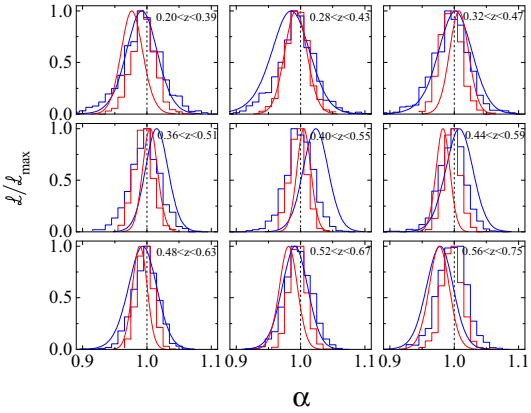

Figure 6. The 1D distribution of the parameter α from the pre-reconstructed mock catalogue (blue histograms), galaxy catalogue (blue curves) and from the post-reconstructed mock catalogue (red histograms), galaxy catalogue (red curves).

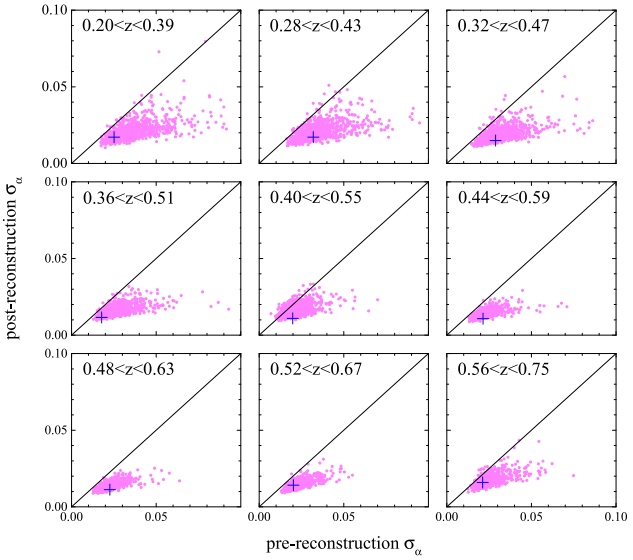

Figure 7. The scatter plot of error of α using pre- and post-reconstruction mock catalogue. Each magenta point denotes the 1σ error of α from each mock (totally 1000 mocks) and the cross (blue) is the error measured by data.

Since our redshift slices are highly correlated within the overlapping range, which is visualized in Fig. 1, it is important to determine the correlations between redshift slices. We repeat the fitting on BAO parameter using each mock measurement, derive the covariance matrix between the ith z bin and jth z bin using $C_{ij} \equiv \langle\alpha_i\alpha_j\rangle - \langle\alpha_i\rangle\langle\alpha_j\rangle$, then calculate the correlation coefficient with $r_{ij} = C_{ij}/\sqrt{C_{ii}C_{jj}}$. The normalized correlations of α between redshift slices, i.e. $\alpha(z_i)$, $i = 1, ..., 9$ for the post-reconstruction are plotted in the left-hand panel of Fig. 11. It is seen that each bin is correlated to the three redshift bins next to it.

6.2 Anisotropic BAO measurements

We present the fitting result on the anisotropic BAO parameters in Table 5 before and after reconstruction. Our measurements on $\alpha_\perp$ and $\alpha_\parallel$ are plotted in terms of redshift in blue squares of Fig. 12.

Based on the input fiducial values for $D_A^{\rm fid}/r_d^{\rm fid}$ and $H^{\rm fid}r_d^{\rm fid}$, we can obtain the constraints on the transverse and radial distance parameters, $D_A(z)/r_d$ and $H(z)r_d$, as listed in Table 6. The measurement precisions are within 2.3–3.5 per cent for $D_A(z)/r_d$ and 3.9–8.1 per cent for $H(z)r_d$ before the reconstruction. Using the reconstructed catalogues, the precisions are improved, which can reach 1.3–2.2 per cent for $D_A(z)/r_d$ and 2.1–6.0 per cent for $H(z)r_d$.

We determine the correlations between overlapping redshift slices using the measurements from mock catalogue. The calculation procedure has described in Section 6.1. The normalized correlated matrix of the parameters, $[\alpha_\perp(z_1), \alpha_\parallel(z_1), ..., \alpha_\perp(z_9), \alpha_\parallel(z_9)]$, between

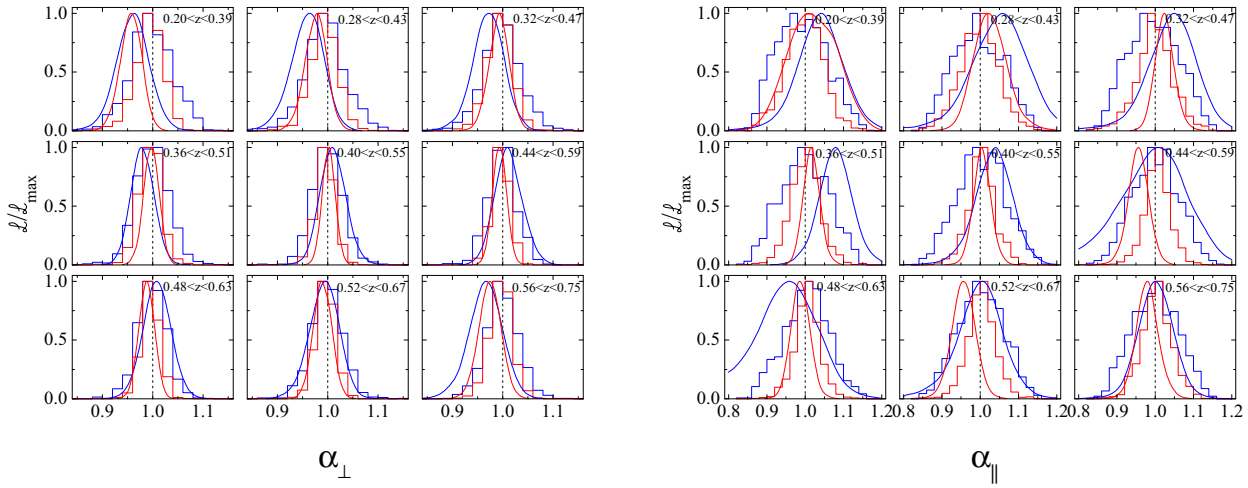

Figure 8. The 1D distributions of the parameters $\alpha_\perp$ (left-hand panel) and $\alpha_{||}$ (right-hand panel) from the pre-reconstructed mock catalogue (blue histograms), galaxy catalogue (blue curves) and from the post-reconstructed mock catalogue (red histograms), galaxy catalogue (red curves).

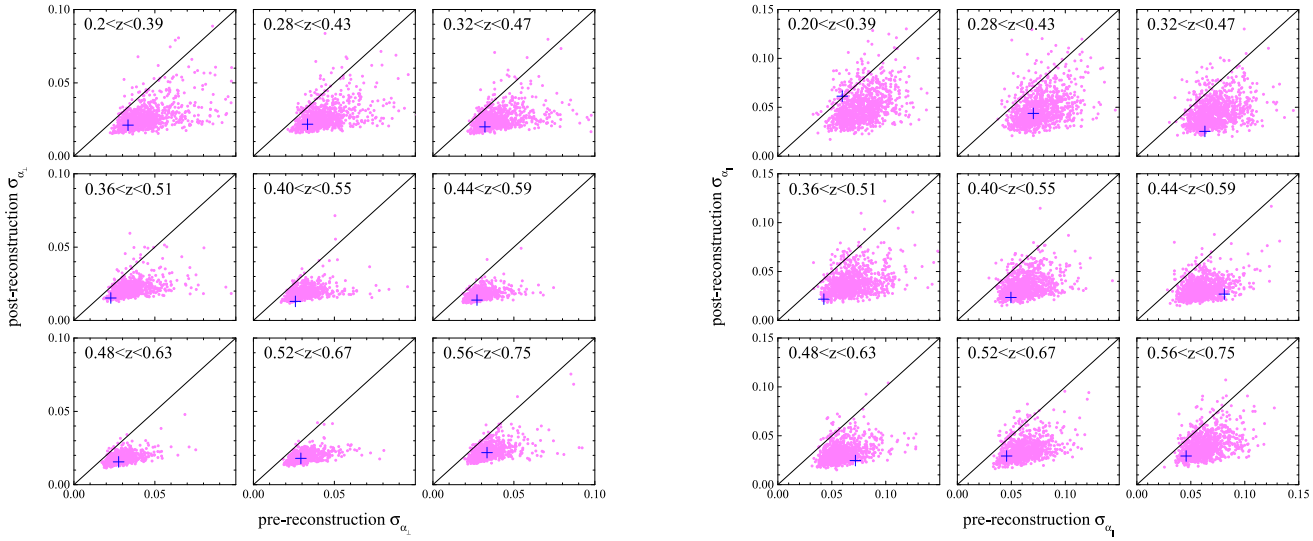

Figure 9. The scatter plots of errors of $\alpha_\perp$ (left-hand panel) and $\alpha_{||}$ (right-hand panel) using pre- and post-reconstruction mock catalogue. Each magenta point denotes the 1σ error from each mock (totally 1000 mocks) and the cross (blue) is the error measured by data.

different redshift slices for the post-reconstruction are plotted in the right-hand panel of Fig. 11.

6.3 Result comparisons

Compared to the Fisher forecast presented in Table 2, the uncertainty on the BAO parameters derived from mocks and data (in Tables 3–5) are generally larger due to the following reasons.

(i) In the Fisher forecast, the probability distribution function (PDF) of parameters are assumed to be Gaussian. However, the PDF for BAO parameters are known to be highly non-Gaussian (Alam et al. 2016), which can in principle dilute the constraints;

(ii) In the Fisher forecast process presented in Section 3, the effects of systematics of observations, including the seeing, extinction, airmass and so on, which are inevitable in the actual observation and BAO measurements, are not taken into account. These effects are accounted for using the 'systematic weights' in the actual data catalogue. We also removed the broad-band shape of the correlation function by marginalizing over the coefficients of the polynomials (see discussions in Section 4.2) to account for other systematic effects. All these can downgrade the BAO constraints in general.

We compare our pre-reconstructed results on the isotropic and anisotropic BAO parameters with the tomographic measurements using the power spectrum in Fourier space (Zhao et al. 2017b). The comparison is plotted in the left-hand panel of Fig. 13. We can see that the isotropic results (blue points) agree well with each other. Because of the high correlations between anisotropic parameters, the comparison looks scattered, especially for the parameter $\alpha_\parallel$. Within the 1σ error, the results are consistent. The main difference is that Zhao et al. (2017b) use the monopole, quadrupole and hexadecapole in the power spectrum, while we do not include the hexadecapole in our pre-reconstruction case. The role of the hexadecapole on anisotropic BAO constraints is discussed in detail (Zhao et al. 2017b).

Table 4. The measurements on the isotropic BAO parameters and the reduced χ^2 using the pre- and post-reconstruction catalogues, respectively.

$z_{\rm eff}$	α	D_V/r_d	χ^2/dof
	Pre-reconstruction		
0.31	0.9916 ± 0.0251	8.31 ± 0.21	12.6/15
0.36	0.9825 ± 0.0320	9.40 ± 0.31	13.2/15
0.40	1.0000 ± 0.0288	10.47 ± 0.30	20.9/15
0.44	1.0155 ± 0.0178	11.56 ± 0.20	16.5/15
0.48	1.0234 ± 0.0198	12.48 ± 0.24	22.3/15
0.52	1.0074 ± 0.0214	13.04 ± 0.28	21.9/15
0.56	0.9924 ± 0.0226	13.55 ± 0.31	22.1/15
0.59	0.9906 ± 0.0202	14.21 ± 0.29	21.0/15
0.64	0.9770 ± 0.0212	14.82 ± 0.32	15.1/15
	Post-reconstruction		
0.31	0.9771 ± 0.0172	8.18 ± 0.14	16.8/15
0.36	0.9925 ± 0.0172	9.50 ± 0.16	12.5/15
0.40	1.0074 ± 0.0149	10.54 ± 0.16	22.0/15
0.44	1.0050 ± 0.0116	11.44 ± 0.13	24.8/15
0.48	1.0051 ± 0.0109	12.26 ± 0.13	39.0/15
0.52	0.9824 ± 0.0108	12.72 ± 0.14	13.8/15
0.56	0.9887 ± 0.0112	13.50 ± 0.15	10.6/15
0.59	0.9808 ± 0.0141	14.07 ± 0.20	13.9/15
0.64	0.9764 ± 0.0159	14.81 ± 0.24	20.7/15

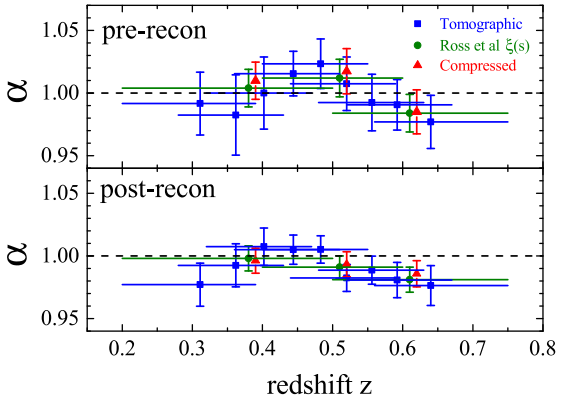

Figure 10. The fitting results on the isotropic BAO parameter, α using the pre- and post-reconstruction catalogues, respectively.

In order to test the consistency between our measurements and the measurements in three redshift bins (Ross et al. 2017), we compressed our measurements into three redshift bins. Namely, we compressed the first four redshift bins, which covers the redshift range from 0.2 to 0.51, into one measurement. The compression is performed by introducing a parameter and fitting it to the measurements in these four redshift bins with their covariance matrix. The fifth and sixth bins ($0.4 < z < 0.59$) are compressed as the second measurement value. The last compressed measurement are from the remaining bins ($0.48 < z < 0.75$). The compression results are shown in red triangles of Figs 10 and 12. In these figures, the green points denote the results within three redshift bins from $\xi(s)$ measurements in Ross et al. (2017), i.e. two bins without overlapping between each other, [0.2, 0.5] and [0.5, 0.75], and an overlapping bin, [0.4, 0.6]. It is seen that with less redshift bins, more precise measurements and much tighter constraints can be obtained. In contrast, dividing more redshift bins in the tomographic case can capture the redshift information of galaxy clustering with more measurements at different effective redshifts. The comparison is plotted in the right-hand panel of Fig. 13. We can see that our results are consistent with the measurements in Ross et al. (2017).

The comparisons of our anisotropic BAO measurements with the three bins consensus measurements in Alam et al. (2016) are shown in Fig. 14, where the black squares are our measurements, and the red points are the consensus result, which are the combined constraints from the correlation function and power spectrum in Alam et al. (2016). The blue bands correspond to the 68 and 95 per cent CL constraints in the ΛCDM using the *Planck* data assuming a ΛCDM model (Planck Collaboration XI 2016). We can see these results are consistent.

7 CONSTRAINTS ON COSMOLOGICAL MODELS

Using our tomographic measurements on Hubble parameters, we perform the *Om* diagnostic, proposed by Zunckel & Clarkson (2008) and Sahni, Shafieloo & Starobinsky (2008) as a consistency check for the ΛCDM model. It is defined as follows:

$$Om(z) \equiv \frac{[H(z)/H_0]^2 - 1}{(1+z)^3 - 1}. \quad (31)$$

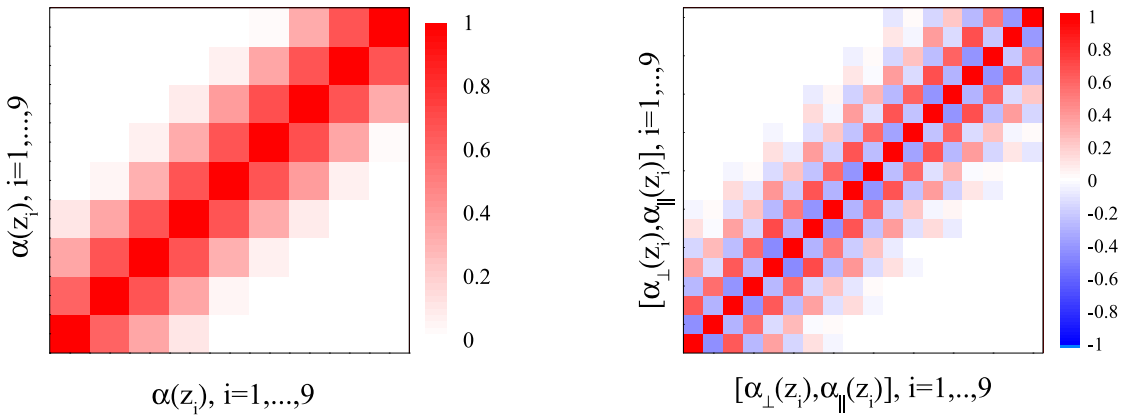

Figure 11. Left-hand panel: the correlation matrix for parameters, $[\alpha(z_1), \alpha(z_2), ..., \alpha(z_8), \alpha(z_9)]$, between different redshift slices. Right-hand panel: the correlation matrix for parameters, $[\alpha_\perp(z_1), \alpha_\parallel(z_1), ..., \alpha_\perp(z_9), \alpha_\parallel(z_9)]$, between different redshift slices.

Table 5. The fitting results on the anisotropic BAO parameters, $\alpha_\perp$ and $\alpha_\parallel$, and their correlation coeffecient r using the pre- and post-reconstruction catalogues, respectively.

	Pre-reconstruction				Post-reconstruction			
$z_{\rm eff}$	$\alpha_\perp$	$\alpha_\parallel$	r	χ^2/dof	$\alpha_\perp$	$\alpha_\parallel$	r	χ^2/dof
0.31	0.9596 ± 0.0334	1.0378 ± 0.0597	−0.40	26.0/30	0.9566 ± 0.0212	1.0203 ± 0.0614	−0.47	38.2/30
0.36	0.9584 ± 0.0334	1.0464 ± 0.0704	−0.30	29.0/30	0.9762 ± 0.0218	1.0275 ± 0.0438	−0.36	35.3/30
0.40	0.9706 ± 0.0321	1.0414 ± 0.0631	−0.27	41.7/30	0.9924 ± 0.0200	1.0250 ± 0.0253	−0.39	34.0/30
0.44	0.9798 ± 0.0228	1.0788 ± 0.0426	−0.41	34.8/30	0.9971 ± 0.0153	1.0168 ± 0.0217	−0.36	27.5/30
0.48	1.0104 ± 0.0259	1.0341 ± 0.0496	−0.42	38.0/30	1.0020 ± 0.0130	1.0050 ± 0.0235	−0.39	35.6/30
0.52	1.0114 ± 0.0272	0.9962 ± 0.0810	−0.57	38.7/30	0.9935 ± 0.0139	0.9560 ± 0.0270	−0.49	12.1/30
0.56	1.0083 ± 0.0276	0.9560 ± 0.0718	−0.51	40.2/30	0.9878 ± 0.0156	0.9877 ± 0.0247	−0.43	16.1/30
0.59	0.9926 ± 0.0293	0.9982 ± 0.0601	−0.53	37.3/30	0.9896 ± 0.0180	0.9564 ± 0.0307	−0.41	26.1/30
0.64	0.9656 ± 0.0334	1.0014 ± 0.0457	−0.43	25.7/30	0.9744 ± 0.0219	0.9794 ± 0.0294	−0.45	33.3/30

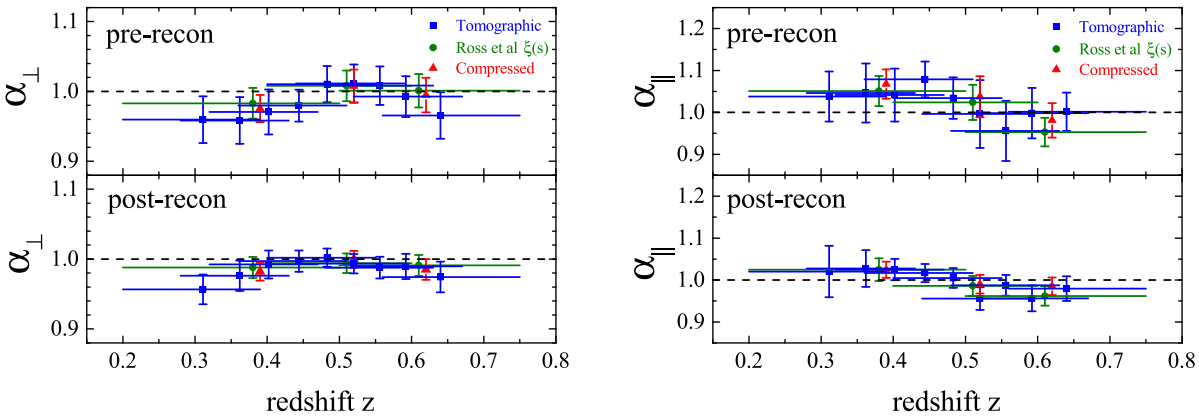

Figure 12. The fitting results on the anisotropic BAO parameters, $\alpha_\perp$ (left-hand panel) and $\alpha_\parallel$ (right-hand panel) using the pre- and post-reconstruction catalogues, respectively.

Table 6. The fitting results on the anisotropic BAO parameters, D_A/r_d and Hr_d using the pre- and post-reconstruction catalogues, respectively.

	Pre-reconstruction	
$z_{\rm eff}$	D_A/r_d	$Hr_d/10^3$[kms^{-1}]
0.31	6.31 ± 0.22	11.35 ± 0.65
0.36	6.96 ± 0.24	11.60 ± 0.78
0.40	7.53 ± 0.25	11.93 ± 0.72
0.44	8.06 ± 0.19	11.81 ± 0.47
0.48	8.71 ± 0.22	12.61 ± 0.60
0.52	9.06 ± 0.24	13.38 ± 1.09
0.56	9.35 ± 0.26	14.25 ± 1.07
0.59	9.48 ± 0.28	13.94 ± 0.84
0.64	9.53 ± 0.33	14.28 ± 0.65
	Post-reconstruction	
0.31	6.29 ± 0.14	11.55 ± 0.70
0.36	7.09 ± 0.16	11.81 ± 0.50
0.40	7.70 ± 0.16	12.12 ± 0.30
0.44	8.20 ± 0.13	12.53 ± 0.27
0.48	8.64 ± 0.11	12.97 ± 0.30
0.52	8.90 ± 0.12	13.94 ± 0.39
0.56	9.16 ± 0.14	13.79 ± 0.34
0.59	9.45 ± 0.17	14.55 ± 0.47
0.64	9.62 ± 0.22	14.60 ± 0.44

In a spatially flat ΛCDM model, $Om(z) = \Omega_m$, which is today's matter density in Universe. In dynamical DE models, $Om(z)$ evolves with redshifts.

Using our measurements of $H(z)r_d$ and combining the fiducial values of $r_d = 147.74$ Mpc and $H_0 = 67.8$ kms^{-1} Mpc^{-1}, we derived $Om(z)$, as shown in Fig. 15, where the blue squares, red points and black triangles denote results using pre-reconstruction tomographic BAO measurements, post-reconstruction tomographic BAO measurements and the DR12 consensus result presented in Alam et al. (2016), respectively.

As a consistency test for the ΛCDM model, we fit constants to the $Om(z)$ values derived from the pre- and post-reconstruction tomographic measurements and 'three $z$bin' consensus measurement. In Fig. 15, we show the best-fitting values in blue, red and black dashed lines and 68 per cent uncertainties in blue, red and grey horizontal bands, respectively. The corresponding results are listed in Table 7. Regarding the goodness-of-fit, the Om measurements in all three cases can be well fitted by constants.[2]

We present the cosmological implications with our tomographic BAO measurements. We use the Cosmomc[3] (Lewis & Bridle 2002) code to perform the fittings on DE parameters in a time-varying DE

[2] Note, however, that the Om estimated from different kinds of data are not consistent (Zhang et al. 2017), which indicates that the ΛCDM model may need to be extended.

[3] http://cosmologist.info/cosmomc/

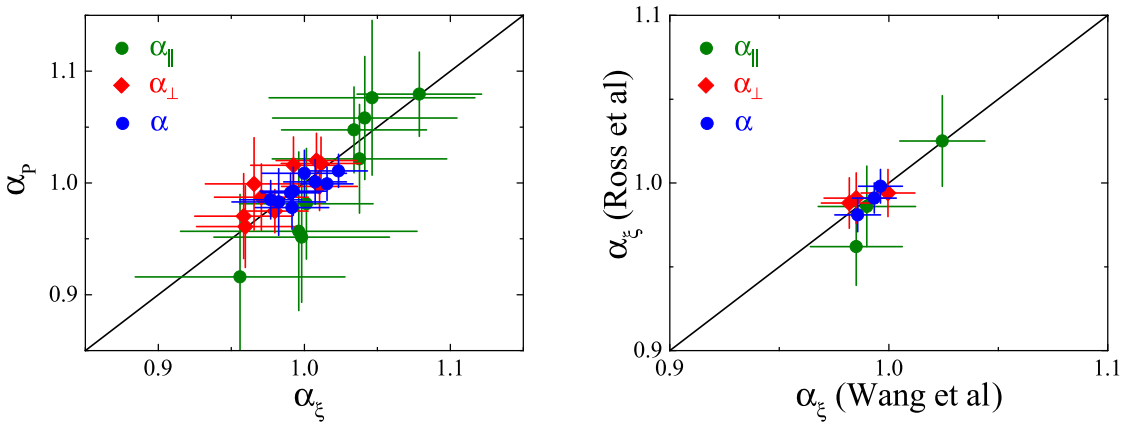

Figure 13. Left-hand panel: the comparison of our result on isotropic and anisotropic BAO parameters from the pre-reconstructed data with that in Zhao et al. (2017b), measured in Fourier space. Right-hand panel: the comparison of our result on isotropic and anisotropic BAO parameters from the post-reconstructed data in the compressed three redshift bins with that in Ross et al. (2017), also measured in configuration space.

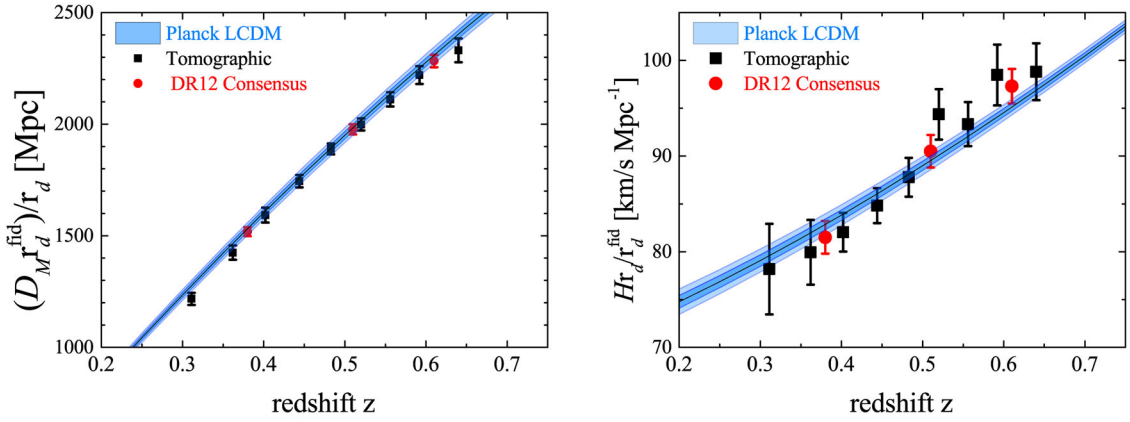

Figure 14. Our tomographic measurements (black squares) on $D_M r_d^{\rm fid}/r_d = (1+z)D_A r_d^{\rm fid}/r_d$ (left-hand panel) and $H(z)r_d/r_d^{\rm fid}$ (right-hand panel) in terms of redshift, compared with the consensus result (red points) in Alam et al. (2016) and the prediction from *Planck* assuming a ΛCDM model (blue bands).

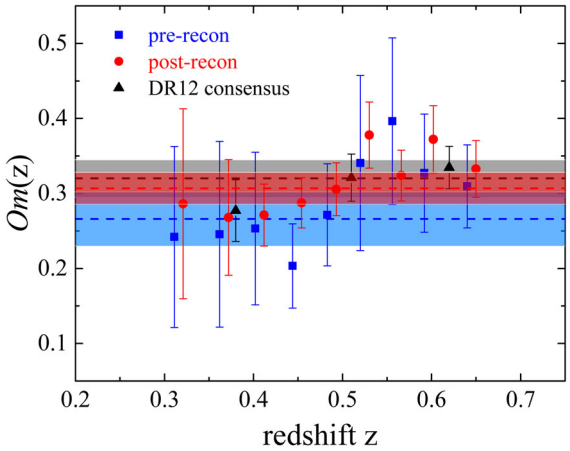

Figure 15. The $Om(z)$ values converted by our measurements on Hubble parameter in nine redshift bins.

with EoS, $w_{\rm DE}(a) = w_0 + w_a(1-a)$ (Chevallier & Polarski 2001; Linder 2003).

We are using the combined data set, including the temperature and polarization power spectra from Planck 2015 data release (Planck Collaboration XI 2016), the 'Joint Light-curve Analysis' (JLA) sample of type Ia SNe (Betoule et al. 2014), the BOSS DR12 BAO distance measurements. We compare the constraining power of different BAO measurements, i.e. tomographic 'nine $z$bin' BAO measurements from the post-reconstructed catalogues, consensus 'three $z$bin' measurements on BAO and RSD in Alam et al. (2016), and the compressed 'one $z$bin' BAO result from the post-reconstruction tomographic measurements.

Table 7. The best-fitting values with 1σ errors and the reduced χ^2 (defined as chi-squared per degree of freedom) using the derived $Om(z)$ from the pre- and post-reconstruction tomographic measurements and 'three $z$bin' consensus measurement, respectively.

Data	Ω_m	χ^2/dof
Pre-recon nine $z$bin	0.266 ± 0.036	4.04/8
Post-recon nine $z$bin	0.307 ± 0.021	7.73/8
DR12 Consensus	0.320 ± 0.025	1.73/2

The results of the parameters w_0 and w_a are presented in Table 8. We can see the uncertainties of parameters are improved with the 'nine $z$bin' BAO measurements in our work.

In $w_0 w_a$CDM, comparing the tomographic 'nine $z$bin' with the non-tomographic 'one $z$bin' results, the errors of w_0 and w_a are

Table 8. Joint data constraints on DE EoS parameters w_0 and w_a in the w_0w_aCDM. Here, we compare the constraining power of the BOSS DR12 BAO measurements, i.e. the tomographic 'nine $z$bin' measurements in this work, consensus 'three $z$bin' measurements in Alam et al. (2016), and the compressed 'one $z$bin' result from tomographic measurements.

Planck+JLA+BOSS	w_0	w_a
Tomographic (nine $z$bin)	-0.957 ± 0.097	-0.389 ± 0.358
DR12 Consensus (three $z$bin)	-0.942 ± 0.101	-0.288 ± 0.359
Compressed (one $z$bin)	-0.917 ± 0.103	-0.589 ± 0.414

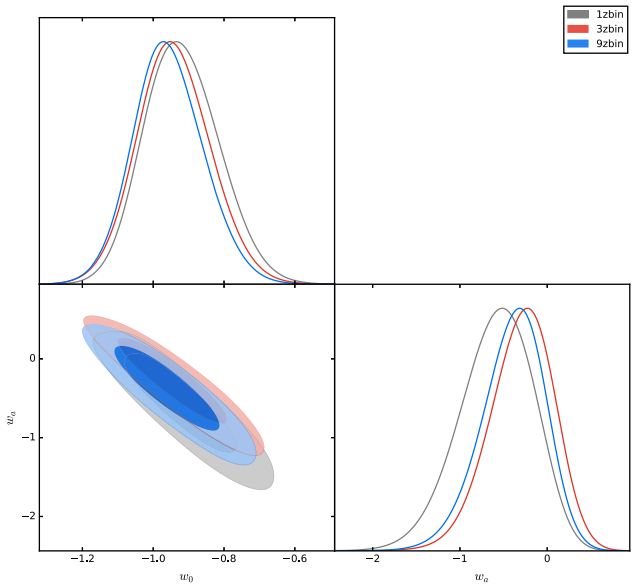

Figure 16. The 1D posterior distribution of w and w_a and their 2D contour plots in the CPL model from the compressed 'one $z$bin' BAO (grey line and contour), consensus 'three $z$bin' BAO and RSD (red line and contour) and tomographic 'nine $z$bin' BAO (blue line and contour).

improved by 6 and 16 per cent, respectively. Using the Figure of Merit (FoM) (Albrecht et al. 2009), which is inversely proportional to the area of the contour as shown in Fig. 16, to quantify this improvement, the FoM is improved by a factor of 1.24 (FoM = 49 for the grey contour from the 'one $z$bin' result and FoM = 61 for the blue contour from the 'nine $z$bin' result in Fig. 16). Comparing the 'nine $z$bin' with 'three $z$bin' results, the 'nine $z$bin' BAO measurement give the slightly tighter constraints.

8 CONCLUSION

Measurements of the BAO distance scales have become a robust way to map the expansion history of the Universe. A precise BAO distance measurement at a single effective redshift can be achieved using the entire galaxies in the survey, covering a wide redshift range. However, the tomographic information is largely lost. To extract the redshift information from the samples, one possible way is to use overlapping redshift slices.

Using the combined sample of BOSS DR12, we perform a tomographic BAOs analysis using the two-point galaxy correlation function. We split the whole redshift range of sample, $0.2 < z < 0.75$, into multiple overlapping redshift slices, and measured correlation functions in all the bins. With the full covariance matrix calibrated using MultiDark-Patchy mock catalogues, we obtained the isotropic and anisotropic BAO measurements.

In the isotropic case, the measurement precision on $D_V(z)/r_d$ from the pre-reconstruction catalogue can reach 1.8–3.3 per cent. For the post-reconstruction, the precision is improved, and becomes 1.1–1.8 per cent. In the anisotropic case, the measurement precision is within 2.3–3.5 per cent for $D_A(z)/r_d$ and 3.9–8.1 per cent for $H(z)r_d$ before the reconstruction. Using the reconstructed catalogues, the precision is improved, which can reach 1.3–2.2 per cent for $D_A(z)/r_d$ and 2.1–6.0 per cent for $H(z)r_d$.

We present the comparison of our measurements with that in a companion paper (Zhao et al. 2017b), where the tomographic BAO is measured using multipole power spectrum in Fourier space. We find an agreement within the 1σ confidence level. The derived three-bin results from our tomographic measurements are also compared to the three-bin measurements in Ross et al. (2017), and a consistency is found.

We perform cosmological constraints using the tomographic nine-bin BAO measurements, the consensus three-bin BAO and RSD measurements, and the compressed one-bin BAO measurement. Comparing the constraints on w_0w_aCDM from nine-bin and one-bin BAO distance measurements, the uncertainties of the parameters, w_0 and w_a are improved by 6 and 16 per cent, respectively. The DE FoM is improved by a factor of 1.24. Comparing the 'nine $z$bin' with 'three $z$bin' results, the 'nine $z$bin' BAO measurement give the slightly tighter constraints.

The future galaxy surveys will cover a larger and larger cosmic volume, and there is rich tomographic information in redshifts to be extracted. The method developed in this work can be easily applied to the upcoming galaxy surveys and the gain in the temporal information is expected to be more significant.

ACKNOWLEDGEMENTS

YW is supported by the NSFC grant no. 11403034. GBZ is supported by NSFC grant no. 11673025, and by a Royal Society-Newton Advanced Fellowship. GBZ and YW are supported by National Astronomical Observatories, Chinese Academy of Sciences and by University of Portsmouth.

Funding for SDSS-III has been provided by the Alfred P. Sloan Foundation, the Participating Institutions, the National Science Foundation, and the US Department of Energy Office of Science. The SDSS-III website is http://www.sdss3.org/. SDSS-III is managed by the Astrophysical Research Consortium for the Participating Institutions of the SDSS-III Collaboration including the University of Arizona, the Brazilian Participation Group, Brookhaven National Laboratory, Carnegie Mellon University, University of Florida, the French Participation Group, the German Participation Group, Harvard University, the Instituto de Astrofisica de Canarias, the Michigan State/Notre Dame/JINA Participation Group, Johns Hopkins University, Lawrence Berkeley National Laboratory, Max Planck Institute for Astrophysics, Max Planck Institute for Extraterrestrial Physics, New Mexico State University, New York University, Ohio State University, Pennsylvania State University, University of Portsmouth, Princeton University, the Spanish Participation Group, University of Tokyo, University of Utah, Vanderbilt University, University of Virginia, University of Washington and Yale University.

This research used resources of the National Energy Research Scientific Computing Center, which is supported by the Office of Science of the U.S. Department of Energy under Contract No. DE-AC02-05CH11231, the SCIAMA cluster supported by University of Portsmouth and the ZEN cluster supported by NAOC.

REFERENCES

Alam S. et al., 2015, ApJS, 219, 12
Alam S. et al., 2016, preprint (arXiv:1607.03155)
Albrecht A. et al., 2009, preprint (arXiv:0901.0721)
Anderson L. et al., 2014, MNRAS, 441, 24
Betoule M. et al., 2014, A&A, 568, A22
Beutler F. et al., 2011, MNRAS, 416, 3017
Beutler F. et al., 2017a, MNRAS, 464, 3409
Beutler F. et al., 2017b, MNRAS, 466, 2242
Blake C. et al., 2011, MNRAS, 418, 1707
Chevallier M., Polarski D., 2001, Int. J. Mod. Phys. D, 10, 213
Chuang C.-H., Wang Y., 2012, MNRAS, 426, 226
Chuang C.-H., Wang Y., 2013, MNRAS, 431, 2634
Chuang C.-H. et al., 2016, preprint (arXiv:1607.03151)
Cuesta A. J. et al., 2016, MNRAS, 457, 1770
Dawson K. S. et al., 2013, AJ, 145, 10
Eisenstein D. J., Hu W., 1998, ApJ, 496, 605
Eisenstein D. J. et al., 2005, ApJ, 633, 560
Eisenstein D. J., Seo H.-J., White M., 2007a, ApJ, 664, 660
Eisenstein D. J., Seo H.-J., Sirko E., Spergel D. N., 2007b, ApJ, 664, 675
Eisenstein D. J. et al., 2011, AJ, 142, 72
Feldman H. A., Kaiser N., Peacock J. A., 1994, ApJ, 426, 23
Gil-Marín H. et al., 2016, MNRAS, 460, 4210
Grieb J. N. et al., 2017, MNRAS
Kaiser N., 1987, MNRAS, 227, 1
Kazin E. A. et al., 2010, ApJ, 710, 1444
Kazin E. A., Sánchez A. G., Blanton M. R., 2012, MNRAS, 419, 3223
Kazin E. A. et al., 2013, MNRAS, 435, 64
Kitaura F.-S. et al., 2016, MNRAS, 456, 4156
Landy S. D., Szalay A. S., 1993, ApJ, 412, 64
Lewis A., Bridle S., 2002, Phys. Rev. D, 66, 103511
Lewis A., Challinor A., Lasenby A., 2000, ApJ, 538, 473
Linder E. V., 2003, Phys. Rev. Lett., 90, 091301
Padmanabhan N., White M., 2008, Phys. Rev. D, 77, 123540
Padmanabhan N., Xu X., Eisenstein D. J., Scalzo R., Cuesta A. J., Mehta K. T., Kazin E., 2012, MNRAS, 427, 2132
Percival W. J., Cole S., Eisenstein D. J., Nichol R. C., Peacock J. A., Pope A. C., Szalay A. S., 2007, MNRAS, 381, 1053
Percival W. J. et al., 2014, MNRAS, 439, 2531
Perlmutter S. et al., 1999, ApJ, 517, 565
Planck Collaboration XI, 2016, A&A, 594, A11
Reid B. A. et al., 2010, MNRAS, 404, 60
Riess A. G. et al., 1998, AJ, 116, 1009
Ross A. J. et al., 2017, MNRAS, 464, 1168
Sahni V., Shafieloo A., Starobinsky A. A., 2008, Phys. Rev. D, 78, 103502
Salazar-Albornoz S., Sánchez A. G., Padilla N. D., Baugh C. M., 2014, MNRAS, 443, 3612
Salazar-Albornoz S. et al., 2017, MNRAS, 468, 2938
Sánchez A. G. et al., 2017a, MNRAS, 464, 1493
Sánchez A. G. et al., 2017b, MNRAS, 464, 1640
Seo H.-J., Eisenstein D. J., 2007, ApJ, 665, 14
Seo H.-J., Beutler F., Ross A. J., Saito S., 2016, MNRAS, 460, 2453
Tegmark M., 1997, Phys. Rev. Lett., 79, 3806
Tegmark M. et al., 2006, Phys. Rev. D, 74, 123507
Vargas-Magaña M. et al., 2016, preprint (arXiv:1610.03506)
Weinberg D. H., Mortonson M. J., Eisenstein D. J., Hirata C., Riess A. G., Rozo E., 2013, Phys. Rep., 530, 87
Xu X., Cuesta A. J., Padmanabhan N., Eisenstein D. J., McBride C. K., 2013, MNRAS, 431, 2834
Zhang Y., Zhang H., Wang D., Qi Y., Wang Y., Zhao G.-B., 2017, RAA, 17, 6
Zhao G.-B. et al., 2017a, preprint (arXiv:1701.08165)
Zhao G.-B. et al., 2017b, MNRAS, 466, 762
Zunckel C., Clarkson C., 2008, Phys. Rev. Lett., 101, 181301

[1]*National Astronomy Observatories, Chinese Academy of Science, Beijing 100012, P. R. China*
[2]*Institute of Cosmology and Gravitation, University of Portsmouth, Dennis Sciama Building, Portsmouth PO1 3FX, UK*
[3]*Instituto de Física Teórica, (UAM/CSIC), Universidad Autónoma de Madrid, Cantoblanco, E-28049 Madrid, Spain*
[4]*Leibniz-Institut für Astrophysik Potsdam (AIP), An der Sternwarte 16, D-14482 Potsdam, Germany*
[5]*Center for Cosmology and AstroParticle Physics, The Ohio State University, Columbus, OH 43210, USA*
[6]*Institut de Ciències del Cosmos (ICCUB), Universitat de Barcelona (IEEC- UB), Martí i Franquès 1, E-08028 Barcelona, Spain*
[7]*Campus of International Excellence UAM+CSIC, Cantoblanco, E-28049 Madrid, Spain*
[8]*Departamento de Física Teórica, Universidad Autónoma de Madrid, Cantoblanco, E-28049 Madrid, Spain*
[9]*Department of Physics and Astronomy, University of Utah, 115 S 1400 E, Salt Lake City, UT 84112, USA*
[10]*Harvard–Smithsonian Center for Astrophysics, 60 Garden St, Cambridge, MA 02138, USA*
[11]*McWilliams Center for Cosmology, Department of Physics, Carnegie Mellon University, 5000 Forbes Ave, Pittsburgh, PA 15213, USA*
[12]*Lawrence Berkeley National Laboratory, 1 Cyclotron Rd, Berkeley, CA 94720, USA*
[13]*Department of Physics, University of California, Berkeley, CA 94720, USA*
[14]*Laboratoire d'Astrophysique, Ecole Polytechnique Fédérale de Lausanne (EPFL), Observatoire de Sauverny, CH-1290 Versoix, Switzerland*
[15]*Department of Chemistry and Physics, King's College, 133 North River St, Wilkes Barre, PA 18711, USA*
[16]*Department of Astronomy and Space Science, Sejong University, Seoul 143-747, Korea*
[17]*Max-Planck-Institut für extraterrestrische Physik, Postfach 1312, Giessenbachstr., D-85741 Garching, Germany*
[18]*Universität Sternwarte Muänchen, Ludwig Maximilian Universität, München, Scheinerstrasse 1, D-81679 Munich, Germany*
[19]*Center for Cosmology and Particle Physics, Department of Physics, New York University, 4 Washington Place, New York, NY 10003, USA*
[20]*School of Physics and Astronomy, University of St Andrews, North Haugh, St Andrews KY16 9SS, UK*
[21]*Instituto de Fisica, Universidad Nacional Autonoma de Mexico, Apdo. Postal 20-364, Mexico*
[22]*Department of Physics, Yale University, New Haven, CT 06511, USA*

This paper has been typeset from a TEX/LATEX file prepared by the author.